Microfabricated PEDOT trilayer actuators: synthesis, characterization, and modeling

Ngoc Tan Nguyen, Cedric Plesse, Frederic Vidal, Caroline Soyer, Sébastien Grondel, John D.W. Madden, Eric Cattan

▶ **To cite this version:**

Ngoc Tan Nguyen, Cedric Plesse, Frederic Vidal, Caroline Soyer, Sébastien Grondel, et al.. Microfabricated PEDOT trilayer actuators: synthesis, characterization, and modeling. SPIE Conference on Electroactive Polymer Actuators and Devices (EAPAD), Mar 2017, Portland, OR, United States. 10.1117/12.2260431 . hal-03280257

HAL Id: hal-03280257

https://hal-uphf.archives-ouvertes.fr/hal-03280257

Submitted on 4 Jul 2022

HAL is a multi-disciplinary open access archive for the deposit and dissemination of scientific research documents, whether they are published or not. The documents may come from teaching and research institutions in France or abroad, or from public or private research centers.

L'archive ouverte pluridisciplinaire **HAL**, est destinée au dépôt et à la diffusion de documents scientifiques de niveau recherche, publiés ou non, émanant des établissements d'enseignement et de recherche français ou étrangers, des laboratoires publics ou privés.

Distributed under a Creative Commons Attribution - NonCommercial| 4.0 International License

Microfabricated PEDOT trilayer actuators: synthesis, characterization, and modeling

Ngoc Tan Nguyen[a,c], Cédric Plesse[b], Frédéric Vidal[b], Caroline Soyer[a], Sébastien Grondel[a], John D.W. Madden[c], Eric Cattan[a]*

[a]Univ. Valenciennes, CNRS, Univ. Lille, ISEN, Centrale Lille, UMR 8520 - IEMN, DOAE, F-59313 Valenciennes, France; [b]Laboratoire de Physicochimie des Polymères et des Interfaces, Université de Cergy-Pontoise, Cergy, France; [c]Advanced Materials and Process Engineering Laboratory, Department of Electrical & Computer Engineering, University of British Columbia, Vancouver, BC, Canada, V6S 1A5

ABSTRACT

Conducting polymer actuators have long been of interest as an alternative to piezoelectric and electrostatic actuators due to their large strains and low operating voltages. Recently, poly (3,4- ethylenedioxythiophene) (PEDOT) – based ionic actuators have been shown to overcome many of the initial obstacles to widespread application in micro-fabricated devices by demonstrating stable operation in air and at high frequencies, along with microfabrication compatible processing using a layer by layer method that does not require any handling. However, there is still a need for characterization, prediction, and control of the actuator behavior. This paper describes the fabrication and characterization of thin trilayers composed of a 7 µm thick solid polymer electrolyte (SPE) sandwiched between two 2.1 µm thick PEDOT-containing layers. Beam properties including capacitance, elastic moduli of the layers, and the extent of charge driven strain, are applied to predict curvature, frequency response and force generation. The actuator is represented by an electrical circuit, a mechanical system described via dynamic beam theory, and a strain-to-charge ratio for the electro-mechanical coupling matrix, which together predict the actuator curvature and the resonant response. The success of this physical model promises to enable design and control of micro-fabricated devices.

Keywords: IEAP micro actuator, PEDOT, layer by layer, force generation, modeling, dynamic beam theory, Bond Graph.

1. INTRODUCTION

Electro active polymers (EAPs) has attracted interest in both academic and industrial fields since their mechanical and electrical characteristics have the potential for widespread application, for instance: locomotion systems [1], steerable micro catheters [2], micro pumps [3-4], micro actuators [5-7]. Poly(3,4-ethylenedioxythiopene) (PEDOT) based-actuators have received a lot of attention due to their properties such as: low density, biocompatibility[8], high stress, high power/weight ratio [9], significant displacement (up to 1%), and low operating voltages [8] in solution or in open-air [10]. They can be electronically controlled with reasonable frequency response and are potentially suitable for microscale applications. Actuating layers have been applied in bilayer [11], trilayer [12-14], and multilayer [15] structures in which conducting polymer electrode (CPE) layers are directly in contact with solid polymer electrolyte (SPE) layers accommodating ion flow. However, due to the large charge fluxes required, and the significant electronic and ionic resistances of CPE and SPE layers, speed of charging and actuation has been slow. These important rate-limiting factors are reducing the response speed of the actuator [16]. A new clean-room compatible process, referred to as Layer-by-Layer (LbL) [17], has been recently been demonstrated which removes the need for manual handling and promises to make the fabrication of conducting polymer actuators highly automated. It also enables thin layers and short device lengths, enabling fast actuation.

In the LbL fabrication process of a trilayer structure, there is a need to creat CPE layers. PEDOT can be polymerized in-situ via electropolymerization [18] or via vapour phase polymerization (VPP) [19]. In the VPP method, PEDOT thin films were fabricated by spin-coating an oxidant solution onto silicon substrate and then exposing this substrate to a monomer vapor.

* eric.cattan@univ-valenciennes.fr;

The interpenetrating polymer network (IPN) situated between two PEDOT electrodes plays a role of an electronic insulator and an ion transfer membrane. For operation in open air, the trilayer actuator needs to be introduced to the electrolyte, which is necessary for the redox process, where during the oxidation and reduction ions flow through the ion transfer membrane. To improve the mechanical properties and ionic conductivity of this SPE, an IPN matrix of two cross-linked polymers: polyethylene oxide (PEO) and nitrile-butadiene rubber (NBR) [14, 20] has been designed and controlled.
For the purpose of control and to predict the actuator's behavior, researchers have developed models. Madden [21] came up with an analytical model based on the diffusive elastic metal phenomenon to describe chemical process between electrolyte and polymer electrode that can be applied to a trilayer actuator, and which was further extended by Shoa [22]. This chemical model was linked to the mechanical deformation by an experimentally determined strain-to-charge ratio – an empirical constant that relates injected ionic charge density to strain [21]. Alici [23] also proposed an analytical model in which emphasizes the effects of the interface between electrolyte and polymer electrode and models it as a capacitor and a resistor.

This previous work has employed equivalent circuit models. A related alternative that is explored here is Bond Graph methodology. It appears to be a promising candidate as it allows easy access to power transformation, stored power, and dissipated power inside these actuators. Bond Graph language has shown its flexibility in working with different energy domains and feasibility to describe interactions between systems [24]. These characteristics provide an approach for the design of actuators and further, the design of complete actuated robots while retaining the physical structure of the model [25]. Few works in modeling IEAP actuators using Bond Graphs have been proposed. Byung-Ju Yi concentrated on diffusion in separator layer and electrodes of ionic polymer-metal composites (IPMCs) and did not describe the mechanical response. The model was not verified by experiments [26]. Nishida developed a more complex model on IPMCs type using distributed port-Hamiltonian [25], while Bowers built a Bond Graph model of bilayer actuators operating in a liquid environment [27]. Since ionic EAP actuators inherently involve energy flow in multiple energy domains: mechanical, electrical, simultaneously with chemical domain, a thorough model for explaining the behavior of this actuator is required. Regarding the work that has been accomplished on fabrication and modeling of trilayer actuators, there is a need to improve the fabrication process and develop a more adaptable model to predict actuator behavior.
Within this work, an improvement in the LbL process to synthesize an ultrathin trilayer structure in a cleanroom environment will be described. A key advance is the precise control of the VPP by using a vacuum heating plate allowing the fine control of pressure and temperature during the process. Following this step, the microbeam dimensions and composition were studied under scanning electron microscope (SEM), via energy-dispersive X-ray (EDX) analysis and through mechanical, electrochemical and electromechanical testing. In next step, an IEAP actuator model is being developed. An RC electrical circuit is represented for physical model, the electromechanical coupling matrix is based on the accepted relationship between the strain and the volumetric charge density (strain is proportional to charge density multiplied by an empirically derived strain to charge ratio), and a mechanical model is coupled in based on the modal superposition method to treat Euler-Bernoulli dynamic beam equations for beam displacement. This model will provide physical insight into IEAP actuator behavior, which should enable designers to optimize the system through identified critical parameters. Furthermore, the model can then be expanded to describe complex actuator geometries and interactions with other systems.

2. EXPERIMENTAL SECTION

2.1 Fabrication

The synthesis of a trilayer actuator is based on the LbL method which was first described by Maziz[28], where all the layers are spin coated and deposited on top of previous layers. The overall process is shown in Fig. 1. In this study, the LbL process has been adapted to clean room compatible microfabrication. The first PEDOT electrode layer was synthesized by mixing Poly(ethylene glycol) methyl ether methacrylate (PEGM) (50 wt. %) and Poly(ethylene glycol) dimethacrylate (PEGDM) (50 wt. %), known as PEO precursors, with Fe(III) p-toluene sulfonate oxidant solution in butanol. PEO precursors were added to this layer, and to all the subsequent layers, and polymerized finally throughout the trilayer structure to improve the adhesion between the layers as well as increase ionic conductivity. A solution was stirred during 10 min and spin coated on a 2-inch silicon wafer. The oxidant solution coated wafer was then placed on a vacuum hot plate for EDOT VPP at 45 ^{o}C for 50 minutes under vacuum. EDOT monomer droplets were placed in the vacuum system on a glass slides situated around the wafer to obtain a homogenous PEDOT layer.

During next step, the SPE layer, based on semi-IPN architecture, was prepared by mixing NBR solution (20 wt. % of NBR and 80 wt. % of cyclohexanone) with PEO precursors (75 wt. % of PEGM and 25 wt. % of PEGDM vs NBR). Free radical initiator dicyclohexyl peroxydicarbonate (DCPD) was then added to the solution, stirred for 15 minutes and degassed. The resulting homogenous blend was spin coated on top of the first PEDOT electrode layer. The wafer was then placed in the vacuum hot plate for 45 min at 50°C under continuous supply of N_2 for pre-polymerization, allowing the PEO network to form in each layer to improve adhesion between those two layers.
The second PEDOT electrode layer was synthesized in the same way as the first one. The oxidant solution was prepared, spin coated on the bilayer, and EDOT VPP was carried out in the vacuum hot plate system the same way as for first electrode. During this step, DCPD (3 wt. % of PEO network) was added into oxidant solution to improve the adhesion between all three layers during final heat treatment.
After EDOT VPP for the second electrode layer, the wafer was placed again in the vacuum hot plate system to polymerize PEO precursors in every layer. The heat treatment time was optimized to be 3 h at 50°C in N_2 environment [17]. During this period, the free radical initiator DCPD initiates the reaction between PEO precursors to form PEO network. PEO precursors in the three layers are crosslinking to increase the mechanical adhesion [29].
The microactuator fabrication includes also a micro-patterning step using laser cutting to obtain desired shape/geometry and a last step where the trilayer was swelled in ionic liquid (EMImTFSI) during one week to integrate ions inside the actuator until it reaches the saturated point (Fig. 1).

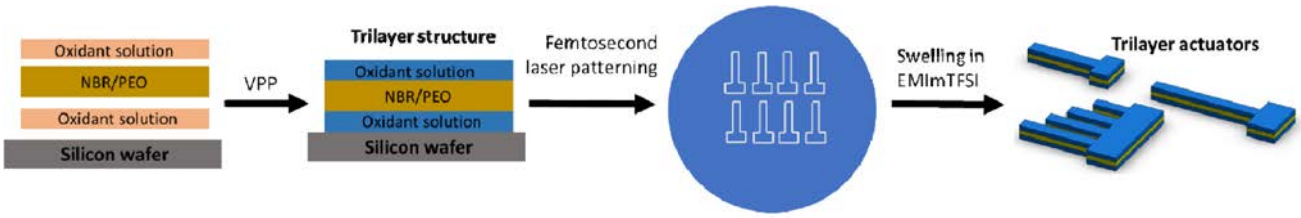

Fig. 1. Micro actuator fabrication process.

2.2 Experimental results

2.2.1 Trilayer structure

Several methods have been developed to pattern the fabricated trilayer such as using a sharp blade, laser patterning, or reactive-ion etching [10, 30]. In our case, a femtosecond laser (Oxford Lasers, UV fundamental 1064 nm wavelength, pulsed length 400 fs, spot size 10 µm, galvanometric mirrors resolution 1µm) was chosen. This tool has enables the minimum dimensions of the actuator to be as low as several hundred micrometers. The thickness of each layer was confirmed using SEM and EDX. Fig. 2a depicts the PEDOT:NBR/PEO:PEDOT trilayer structure showing layer thicknesses of 2.1 µm, 7.0 µm, and 2.1 µm, respectively. The three layers are also shown in Fig. 2b. The sulfur in the PEDOT chains is highlighted in green, and the carbon in NBR/PEO layer is highlighted in red. The thicknesses of the trilayer before and after immersion in EMImTFSI are listed in Table 1.

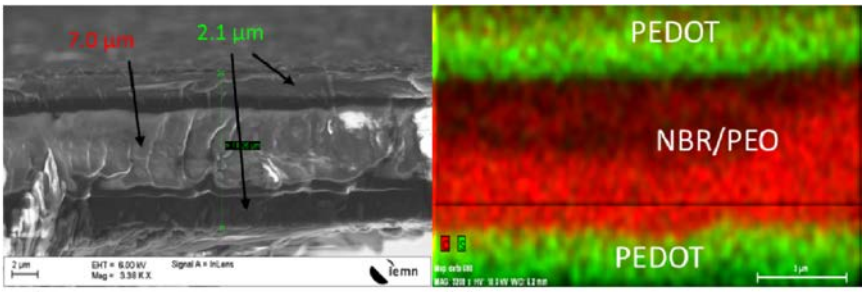

Fig.2. S he trilayer actuator, a) SEM image showing the three layers 2.1 µm, 7.0 µm, and 2.1 µm thick, b) EDX image confirming the separation of the three layers, the sulfur in the PEDOT chains is green and the carbon in the NBR/PEO layer is red (not to scale).

Table 1. Thicknesses of each actuator layer before and after swelling in EMImTFSI

Trilayer	Thickness before swelling (µm)	Thickness after swelling (µm)
Bottom CPE layer	2.1	3.4
SPE layer	7.0	11.5
Top CPE layer	2.1	3.4

2.2.2 Trilayer actuator characterization

In this section, the electrochemical properties and the mechanical properties of the trilayer actuator are presented. The volumetric capacitance, the electronic conductivity of the CPE layers, and the ionic conductivity of the trilayer actuator play an important role in actuation performance. They are also the critical parameters in actuator modeling.

2.2.2.1 Volumetric capacitance

The apparent volumetric capacitance is influenced by the scanning rate of applied voltage. This volumetric capacitance is determined by a cyclic voltammetry using a three-electrode system (Solartron potentiostat, ModuLab XM ECS). In this setup, the counter electrode was a platinum plate with a surface area greater than that of the working electrode, the reference electrode was made of Ag/AgCl, and the working electrode was an actuator held with a platinum clamp. All three electrodes were immersed in EMImTFSI. Capacitance per volume is determined from the relation current-voltage (I-E) curve, scanning rate, and the volume of CPE layers. During this experiment, the potential was swept from -0.6 V to 0.7 V at scan rates from 5 mV/s to 1000 mV/s.

The capacitance was derived from equation $C_{PEDOT} = \frac{\int i(V)dV}{2\vartheta(V_2 - V_1)}$ (F), where ϑ is the scan rate (mV/s), V_1, and V_2 are the lowest and the highest values in the potential window. The volumetric capacitance was calculated using equation $C_V = \frac{C_{PEDOT}}{2Lbh}$ (F/m^3), where L, b, and h are the length, width, and thickness of one electrode.

As described in Fig. 3, the accessible volumetric capacitance varies with the scan rate. This value drops gradually from 53x10^6 F/m^3 to 7x10^6 F/m^3 when the scan rate increases from 5 mV/s to 1000 mV/s.

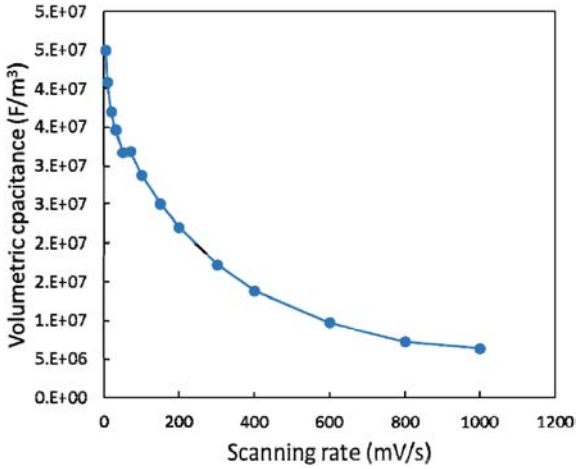

Fig.3. etric capacitance of PEDOT electrodes obtained in EMImTFSI ionic liquid within a potential window of -0.6 V to +0.7 V at scan rates of: 5 mV/s, 10 mV/s, 20 mV/s, 30 mV/s, 50 mV/s, 70 mV/s, 100 mV/s, 200 mV/s, 300 mV/s, 400 mV/s, 600 mV, 800 mV/s, and 1000 mV/s.

2.2.2.2 Ionic conductivity of SPE layer

In this section, a method to determine the ionic conductivity of the SPE layer is described, which is important to determine the magnitude of this rate limiting property. he measurement procedure employs the setup shown in Fig. 4 in which the actuator clamp was made from two gold coated glass slides. An electrical equivalent circuit model of the trilayer actuator was then developed for trilayer actuator. This model included capacitors representing for electrodes, C_P, ionic resistance of the SPE layer, R_S, and short resistance, R_{short}, due to PEDOT layers penetrating into the SPE layer and creating an electronic conduction path between the two electrode layers.

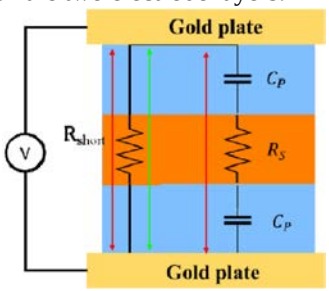

Fig. 4. t traveling direction in the actuator placing between two gold coated glass slides at DC applied voltage (green arrow) and high frequency (red arrows).

At high frequencies, the capacitors, representing ionic storage in the electrode layers, will act as short circuits and the current travelling between two gold plates is described in the red lines. However, when a DC voltage is applied instead of the high frequency voltage, if this voltage is maintained long enough until the capacitors in electrode layers are fully charged, these capacitors will then act as open circuits and the current goes between two gold plates via R_{short}. The resistance in each case can be found via the relation between the current measuring by an ampere meter and the magnitude of the applied voltage.

Finally, the ionic conductivity of SPE layer is $\sigma_{SPE} = \frac{h_S}{R_S L b} = 0.00028\, S/cm$, where h_S, L, and b are the thickness, length, and width of the SPE layer.

2.2.2.3 Electronic resistance of PEDOT layers

To measure the electronic conductivity of a surface, the common device is four-point probe. However, in case of an ultrathin film, this device could damage the measured layer because of its shaping probes. A four-line probe, made from copper foil which is a low resistant material and deposited on a glass slide, for measurement the electronic conductivity of a surface, is described previously by Farajollahi [31]. In this setup, a current is produced by applying a source of voltage between two external copper lines, the voltage between two internal lines was then measured. Knowing distance d between two internal lines, thickness of electrode layer, the applied current and the measured voltage, the electronic conductivity can be derived.

The electronic conductivity measurements of CPE layers had been performed on both the top and bottom electrode layers. As the applied DC voltage changes its value, the current travelling through the closed circuit varies. The current was recorded, and the voltage between the two internal copper lines was collected in order to estimate resistance.

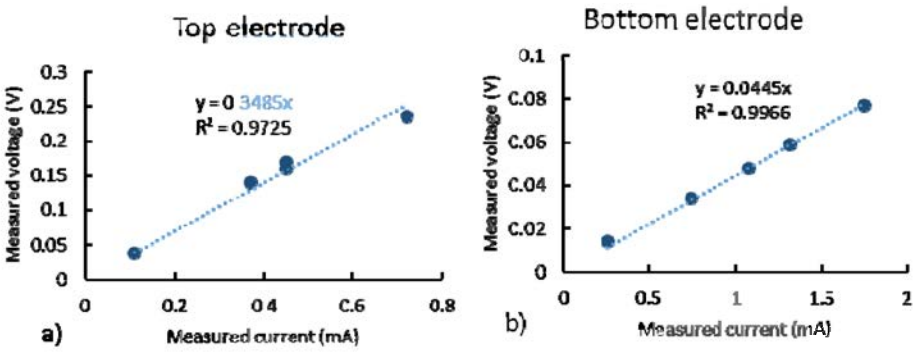

Fig. 5. Four-lin ˛robe measurement of the relation between voltage and current a) Top PEDOT electrode, b) Bottom PEDOT electrode.

As can been seen in Fig. 5, the curves showed a linear relationship between the measured current and the measured voltage, suggesting the electronic resistances of CPE layers is consistent with the effect of a changing voltage. From these relationship, the electronic conductivities can be derived as the following formula, $\sigma_e = \frac{d}{h_{CPE} R_e b}$, where σ_e is electronic conductivity, R_e is the slope of the trend lines in Fig. 5a, b, d is the distance between the two internal copper lines, b is width of the actuator, and h_{CPE} is the thickness of CPE layers. The electronic conductivity of the bottom PEDOT electrode is *32.8 S/cm* while that of the top PEDOT electrode is considerably smaller at *4.62 S/cm.*

2.2.2.4 Young's modulus measurement

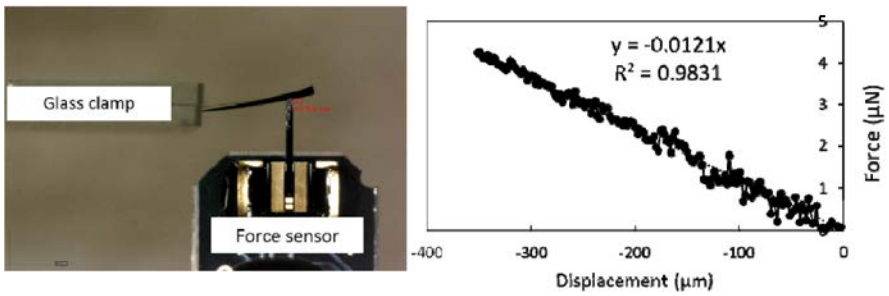

Fig. 6. Young modulus measurement at three different positions on the actuator.

The measurement of the actuator's Young's modulus was performed by applying a force to an actuator. From the measurement, the relation between the applied force and the actuator's displacement was captured by the force sensor (Fig. 6). The effective Young's modulus can be then derived from the equation: $E = \frac{F}{w}\frac{L_m^3}{3I}$, where F is the applied force, L_m is the length between the clamp and the force sensor, w is the beam displacement value, and I is the inertial moment of the beam. This inertial moment is calculated as $I = \frac{bh^3}{12}$, where b is the width, and h is the total thickness of the beam. The results show the consistency of the Young's modulus value in term of positions along the length of the beam, approximately 610±24 MPa.

2.2.2.5 Damping ratio

In mechanical the model, the natural frequency and damping coefficient are useful for determining response at frequencies where inertia is important. These were determined using a vibration experiment. In this experiment, the actuator was fixed at one end and free at the other end. This actuator was then pulled by a micro-beam sensor and quickly released for free vibration. Oscillation was measured directly using a Keyence laser sensor (Keyence LK-G32, measurement range: ±4.5 mm, resolution: 0.05 μm). Damped oscillation is shown in Fig. 7.

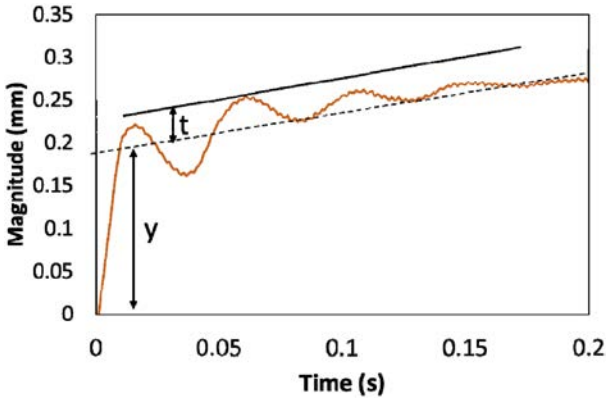

Fig. 7. Beam variation as function of time.

This response suggests that the actuator is well represented as a second-order system system[32]. After subtracting the damping coefficient was calculated using the formula below:

$$\zeta = \frac{1}{\sqrt{\left(\frac{\pi}{ln\left(\frac{t}{y}\right)}\right)^2 + 1}} = 0.39 \quad , \tag{1}$$

where *t* is overshoot amplitude, which is the distance from middle line of sinusoidal part to highest peak and *y* is total displacement. There may be a second, longer time response, given the longer time rise to steady state. This was not included in the model.

Table 2. Actuator parameters

Parameters	Top CPE layer	SPE layer	Bottom CPE layer
Volumetric capacitance	52±0.4x10^6 F/m^3 (frequency of applied voltage ≤ 0.1 Hz) 2±0.2x10^6 F/m^3 in other case		
Ionic conductivity of SPE layer		0.00028 S/cm	
Electronic conductivities	4.62 S/cm		32.8 S/cm
Density	2007±50 (kg/m^3)		
Young modulus	610±24 MPa		
Damping ratio	0.39		
Strain-to-charge ratio	6.10^{-11}(m^3/C)		

3. MODELING TRILAYER ACTUATORS

3.1 Modeling trilayer actuators

3.1.1 Word Bond Graph model of EAP actuators

The proposed model of this actuator consists of three sub systems: the electrical sub system, the electro-mechanical coupling, and the mechanical sub system. The connections between these sub systems are shown in Fig. 8. The input to the global system is voltage $U(t)$ and the outputs are current $i(t) = dQ/dt$, and beam displacement $w(x,t)$. The electrical system outputs the current $i(t)$ to the electro-mechanical coupling system. The mechanical system is driven by the modal actuation force $F(L,t)$, which results from the coupling. Here the force is that generated at the tip, but this could be generalized. The pairs of inputs and outputs (voltage/current, force/velocity) provide information about power transmission.

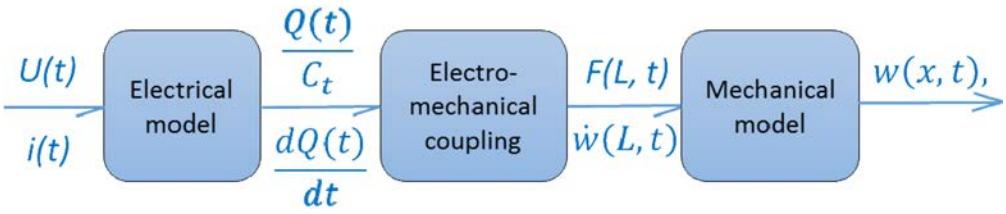

Fig. 8. Global word Bond Graph model of ionic EAP actuator.

3.1.2 Bond Graph model of EAP actuators

Once the word Bond Graph is obtained, the Bond Graph describing each subsystem can be derived from the equations involving in the electrical, the coupling, and the mechanical variables.

3.1.2.1 Electrical model

In this work, we start by employing relatively simple models for each component, and justify these choices based on predictive ability. The electrical model represents the response to the applied voltage under the form of current. The applied voltage is used to promote change in oxidation state inside the conducting polymer electrodes, leading to insertion or removal of charge, and a change in electrode volume. Since the model is designed for thin ($18\ \mu m$) actuators and quite low frequency operation ($\leq 40\ Hz$), the electrodes are represented by one capacitor (Fig. 4). This model has been shown, in some cases, to be sufficient to provide a good description of oxidation rate or in other words, the electrical response of conducting polymer [33-34]. The SPE layer of conducting polymer actuator can be modeled as a resistance R_S which depends on the ionic conductivity and dimensions of SPE. Accordingly, the simple electrical equivalent circuit of EAP actuators consists of resistance R_S and the series of capacitors C_P. This part is described by the following equation:

$$U(t) = \frac{1}{C_t(t)} \int i(t)dt + R_S.i(t) \tag{2}$$

3.1.2.2 Electro-mechanical coupling

Based on the relationship between total force $F(L,t)$ and total charge in the electrodes $Q(t)$, the coupling matrix of $2x2$ elements is established as follows:

$$\begin{bmatrix} U_P(t) \\ F(L,t) \end{bmatrix} = \begin{bmatrix} \frac{1}{C_t(t)} & 0 \\ \frac{\alpha E_P(h_S+h_P)}{2L^2} & 0 \end{bmatrix} \begin{bmatrix} Q(t) \\ w(x,t) \end{bmatrix}, \tag{3}$$

where $U_P(t)$ is the total voltage applied, α is strain to charge ratio[35], E_P is the Young's modulus of the CPE layer, and $w(x,t)$ is tip displacement in the vertical direction at position x along the length of actuator. This model does not consider the sensor response (e.g. effect of externally applied displacement on voltage), which is known to be small[36].

3.1.2.3 Mechanical model

The force generation from coupling effects results in bending of the actuator. Since ionic EAP actuators have a small ratio between thickness and length $\left((2h_P + h_S)/L \ll 1\right)$, this can be considered as a thin beam. Moreover, this type of actuator operates at quite low frequency $(f_{max} \leq 40\ Hz)$, so in this case, Euler-Bernoulli beam theory is perfectly suitable in term of accuracy, computational simulation, and time saving, to predict beam dynamic behavior [34, 37]. Other possible methods not used here include Rayleigh, Shear, and Timoshenko.

In this section, an accurate model, low-order, lumped-parameter representation of distributed elements to describe beam displacement based on Euler-Bernoulli beam theory is given. The number of suitable retaining modes and the incorporation of the beam's damping ratio are also explained.
Karnopp [38] introduced the first model Bond Graph to describe results of solving Euler-Bernoulli beam equation using separation of variables method. A similar method can be used to derive the ionic EAP actuator model in this paper, but with different boundary conditions. The Euler-Bernoulli equation for dynamic beam is adapted as follows:

$$EI\frac{\partial^4 w(x,t)}{\partial x^4} + \rho A\frac{\partial^2 w(x,t)}{\partial t^2} = F(L,t) \quad , \tag{4}$$

where EI is equivalent flexural rigidity of trilayer actuators which is calculated as follows:

$$EI = 2b\left(\frac{h_P^3}{3}E_P + \frac{(h_S/2)^3 - h_P^3}{3}E_S\right). \tag{5}$$

Here E_S is SPE layer's Young's modulus, while A and b are cross section and width of the beam, respectively.
The set of boundary conditions for an ionic EAP beam with clamping at one end are:

$$w(x,t)|_{x=0} = 0; \left.\frac{\partial w(x,t)}{\partial x}\right|_{x=0} = 0 \quad . \tag{6}$$

In the case of an applied point force at the other free end:

$$\left.\frac{\partial^2 w(x,t)}{\partial x^2}\right|_{x=L} = 0 \; ; -EI\left.\frac{\partial^3 w(x,t)}{\partial x^3}\right|_{x=L} = F(t) \quad . \tag{7}$$

The separation of variables method begins by assuming the displacement $w(x,t)$ can be separated into a function of x only , $Y(x)$ and a function of time, t, $\mu(t)$:

$$w(x,t) \; = \; Y(x)\,\mu(t) \quad . \tag{8}$$

Substituting (8) into (6), the solution for this equation is in form of mode shape functions:

$$Y_n(x) = \big(cos\,(r_nL) - cosh(\,r_nL)\big)\big(sin(\,r_nx) + sinh(\,r_nx)\big) - \big(sin(\,r_nx) - sinh(\,r_nx)\big)\big(cos\,(r_nL) + cosh(\,r_nL)\big) \quad , \tag{9}$$

and the contribution of n^{th} mode is:

$$m_n\ddot{\mu_n}(t) + 2\zeta_n\omega_n m_n\dot{\mu_n}(t) + m_n\omega_n^2\mu_n(t) = F(t)Y_n(L), \tag{10}$$

where r_nL yields equation: $cos\,(r_nL)cosh(\,r_nL) = 1$, mode frequencies $\omega_n^2 = \frac{EI}{\rho A}\frac{(r_nL)^4}{L^4}$, mode mass $m_n = \int_0^L \rho A Y_n^2 dx$, and model damping $b_n = 2\zeta_n\omega_n m_n$ in which damping ratio ζ_n is found by experiment. The model stiffness is given by: $k_n = m_n\omega_n^2$.
Once mode shape functions $Y_n(x)$ and contribution functions $\mu_n(t)$ have been determined, equation (8) can be rewritten as: $w(x,t) = \sum_{n=1}^{\infty} Y_n(x)\mu_n(t)$, or in differential form:

$$\dot{w}(x,t) \; = \sum_{n=1}^{\infty} Y_n(x)\dot{\mu_n}(t) \; . \tag{11}$$

3.1.2.4 The global model of actuator

In three previous sections, the physical model, the electro-mechanical coupling, and the mechanical model have been built. To form the global model, it is a matter of connecting all three sub models by bond elements in a Bond Graph. The elements in the model are organized and divided into small subsystems as depicted in Fig. 9.

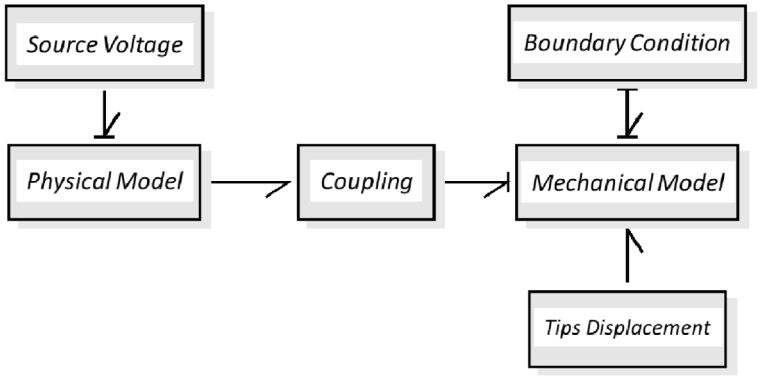

Fig. 9. Ionic EAP actuator's Bond Graph global model.

3.2 Matching of the simulations and experiments

The beam model has now been described and the properties of the beam characterized. In the next step, the beam properties are inserted into the model and simulations are performed. These are compared with measured beam responses to demonstrate the model accuracy. From the model, the value of current passing through the actuator and the displacement at any position along the actuator was derived to compare with experimental results, shown in Fig. 10. The match between both current and displacement is generally within 10 %.

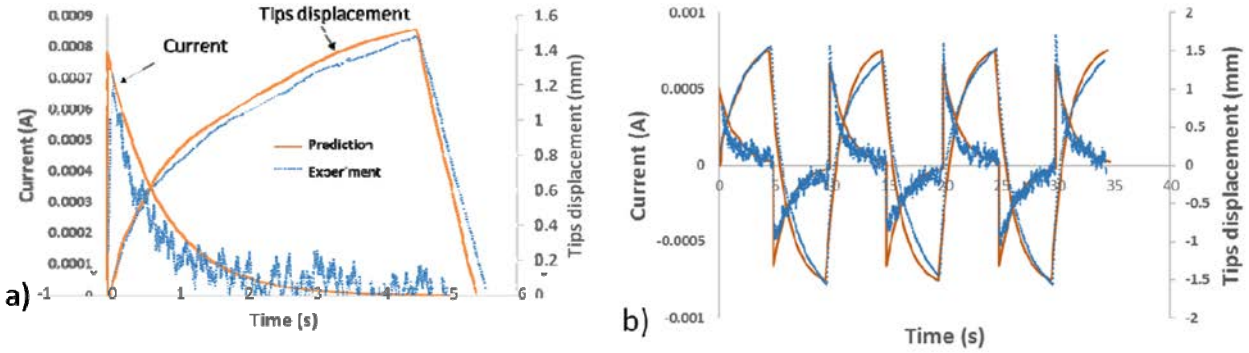

Fig. 10. The current and the tip displacement in response to a 2V step input in a) the half of a cycle, b) in consecutive cycles.

Fig.11a describes the time response of tip displacement as input step voltage is increased from 1 V to 3 V. In this experiment, only the tip movement of a half of voltage changing period was captured due to the symmetry of trilayer structure, as shown in Fig. 10b. It is worth to noting that a sample with high symmetry, resulting in beam symmetric displacement, without internal strain or stress was fabricated using layer by layer method as mentioned in previous section, while in a lot of sample fabricated with a traditional method, there is some internal stress induce a non-symmetric motion. As can be seen, the predictions at low voltage input (< 2 V) matched experimental results. However, the inaccuracy increases when the voltage goes up to 3 V. In general, the given error between predicted and measured behavior is smaller than 5% The correspondence between the prediction and the simulation is confirmed in the curvature results shown in Fig. 11b. The curvature value, which was determined via maximum tip displacement using the equation reported by Sugino [39], rapidly increases from 30 m^{-1} to 65 m^{-1} when voltage rises from 1 V to 2.5 V in total, then this value slightly goes up to 70 m^{-1} as voltage reaches 3 V.

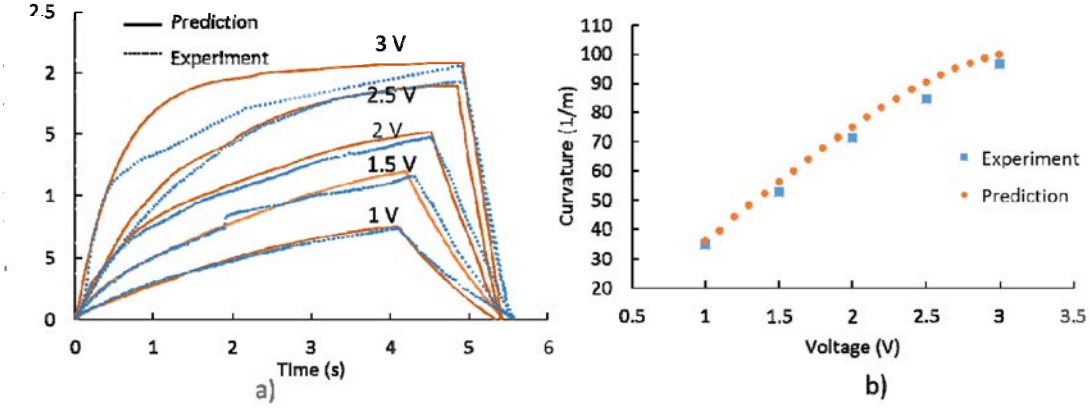

Fig. 11. Beam displacement as the function of voltage. a) Comparison time response of tip displacement between simulation and experiment at several applied voltages; b) Beam curvature as function of voltage changes.

Another set of experiments were performed to verify the model in the condition of varied frequency. While square wave voltage amplitude was kept at 2 V in total, the input frequency changed from 0.1 Hz to 40 Hz. As can be seen in Fig. 12, the model proves to have good ability to predict curvature as a function of frequency. Both experimental and simulated curvature rapidly decrease to 2 m^{-1} at 5 Hz from 67 m^{-1} at 0.1 Hz. As frequency continues to rise up to 40 Hz, the curvature approaches zero.

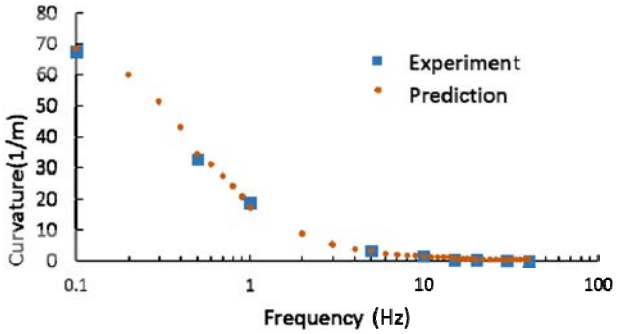

Fig. 12. Beam curvature as function of applied frequencies.

The model has been shown to provide reasonable simulations, particularly at lower applied voltages (< 2.5 V). This model also helps describe the shape of the beam as it bends for example. Here we predict dynamic behavior of the beam as shown in Fig. 13a. At 2 V of magnitude and 0.1 Hz of frequency, considering only a half cycle of applied voltage, the beam decreases its movement speed as it approaches the maximum displacement state. This phenomenon comes from the effect of the capacitor which slows down its charging speed when as it approaches maximum charging voltage. The beam displacement values at different positions can also be derived as shown in Fig. 13b. While input voltage varied between 0 and 3 V and the frequency was constant at 0.1 Hz, beam displacement values in vertical direction at position of $w(x = 0;\ 1.4;\ 2.8;\ 4.2;\ 5.6;\ 7)\ mm$ were collecting in simulation results. It should be noted that the Euler-Bernoulli dynamic beam theory does not consider beam displacement in horizontal direction as it is relatively smaller compared to that in the vertical direction. In other words, the beam shape at different positions along the beam length remains at the same horizontal position during its displacement.

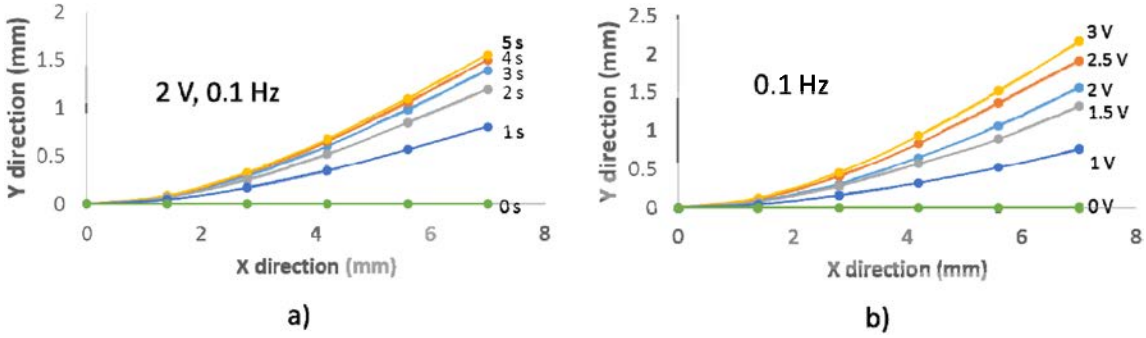

Fig. 23. Beam shape in: a) dynamic behavior of the beam; b) magnitude of applied voltage.

4. CONCLUSION

This paper presents the layer by layer method of fabricating microactuators. The actuators have been characterized to find out the relationship between the performance parameters. The actuator's properties, such as electrochemical properties: volumetric capacitance, electronic conductivity of the electrode layers, ionic conductivity of the SPE layer, the electromechanical coupling, and the mechanical properties: Young's modulus, damping ratio, have been characterized. In addition, a simple model including: an electrical equivalent circuit, a coupling element, and a mechanical model based on Euler Bernoulli dynamic beam theory, has been established. An agreement between simulation and experimental results shows the model's ability in predicting the actuator behavior. In general, the model can be used as an effective tool to optimize the design of the trilayer actuator.

ACKNOWLEDGMENTS

This project received funding from the European Union's Horizon 2020 research and innovation program under the Marie Skłodowska-Curie grant agreement No 641822 - MICACT. This work was partly supported by the French Government through the National Research Agency (ANR) under program PIA EQUIPEX LEAF (ANR-11-EQPX-0025), RENATECH, MICRO-TIP projects, and Natural Sciences and Engineering Research Council of Canada.

REFERENCES

[1] S. McGovern, G. Alici, V. T. Truong *et al.*, "Finding NEMO (novel electromaterial muscle oscillator): A polypyrrole powered robotic fish with real-time wireless speed and directional control," Smart Materials and Structures, 18(9), (2009).

[2] A. Della Santa, A. Mazzoldi, and D. De Rossi, "Steerable microcatheters actuated by embedded conducting polymer structures," Journal of Intelligent Material Systems and Structures, 7(3), 292-300 (1996).

[3] S. Ramírez-García, and D. Diamond, "Biomimetic, low power pumps based on soft actuators," Sensors and Actuators, A: Physical, 135(1), 229-235 (2007).

[4] Y. Wu, D. Zhou, G. M. Spinks *et al.*, "TITAN: A conducting polymer based microfluidic pump," Smart Materials and Structures, 14(6), 1511-1516 (2005).

[5] S. A. Wilson, R. P. J. Jourdain, Q. Zhang *et al.*, "New materials for micro-scale sensors and actuators. An engineering review," Materials Science and Engineering R: Reports, 56(1-6), 1-129 (2007).

[6] D. Pede, E. Smela, T. Johansson *et al.*, "A general-purpose conjugated-polymer device array for imaging," Advanced Materials, 10(3), 233-237 (1998).

[7] R. Kiefer, X. Mandviwalla, R. Archer *et al.*, "The application of polypyrrole trilayer actuators in microfluidics and robotics." 6927.

[8] E. Smela, "Conjugated Polymer Actuators for Biomedical Applications," Advanced Materials, 15(6), 481-494 (2003).

[9] A. Mazzoldi, A. D. Santa, and D. De Rossi, [Conducting Polymer Actuators: Properties and Modeling] Springer Berlin Heidelberg, Berlin, Heidelberg(2000).

[10] A. Khaldi, C. Plesse, C. Soyer *et al.*, "Conducting interpenetrating polymer network sized to fabricate microactuators," Applied Physics Letters, 98(16), (2011).

[11] M. S. Cho, H. J. Seo, J. D. Nam *et al.*, "A solid state actuator based on the PEDOT/NBR system," Sensors and Actuators, B: Chemical, 119(2), 621-624 (2006).

[12] J. Citerin, A. Kheddar, M. Hafez *et al.*, "Characterization of a new interpenetrated network conductive polymer (IPN-CP) as a potential actuator that works in air conditions." 1, 913-918 vol.1.

[13] U. L. Zainudeen, M. A. Careem, and S. Skaarup, "PEDOT and PPy conducting polymer bilayer and trilayer actuators," Sensors and Actuators, B: Chemical, 134(2), 467-470 (2008).

[14] C. Plesse, F. Vidal, H. Randriamahazaka *et al.*, "Synthesis and characterization of conducting interpenetrating polymer networks for new actuators," Polymer, 46(18), 7771-7778 (2005).

[15] K. Ikushima, S. John, K. Yokoyama *et al.*, "A practical multilayered conducting polymer actuator with scalable work output," Smart Materials and Structures, 18(9), (2009).

[16] J. D. M. Tina Shoa, Chi-Wah Eddie Fok, Tissaphern Mirfakhrai, "Rate Limits in Conducting Polymers," Advances in Science and Technology, 61, 7 (2008).

[17] A. Maziz, C. Plesse, C. Soyer *et al.*, "Top-down Approach for the Direct Synthesis, Patterning, and Operation of Artificial Micromuscles on Flexible Substrates," ACS Appl Mater Interfaces, 8(3), 1559-64 (2016).

[18] J. F. Hulvat, and S. I. Stupp, "Liquid-crystal templating of conducting polymers," Angew Chem Int Ed Engl, 42(7), 778-81 (2003).

[19] B. Winther-Jensen, D. W. Breiby, and K. West, "Base inhibited oxidative polymerization of 3,4-ethylenedioxythiophene with iron(III)tosylate," Synthetic Metals, 152(1), 1-4 (2005).

[20] F. Vidal, C. Plesse, G. Palaprat *et al.*, "Conducting IPN actuators: From polymer chemistry to actuator with linear actuation," Synthetic Metals, 156(21–24), 1299-1304 (2006).

[21] J. D. W. Madden, [Conducting polymer actuators] Massachusetts Institute of Technology, (2000).

[22] T. Shoa, J. D. Madden, N. R. Munce *et al.*, “Analytical modeling of a conducting polymer-driven catheter,” Polymer International, 59(3), 343-351 (2010).
[23] G. Alici, B. Mui, and C. Cook, “Bending modeling and its experimental verification for conducting polymer actuators dedicated to manipulation applications,” Sensors and Actuators, A: Physical, 126(2), 396-404 (2006).
[24] D. Karnopp, [System dynamics : modeling and simulation of mechatronic systems] Wiley, Hoboken(2012).
[25] G. Nishida, K. Takagi, B. Maschke *et al.*, “Multi-scale distributed parameter modeling of ionic polymer-metal composite soft actuator,” Control Engineering Practice, 19(4), 321-334 (2011).
[26] B. J. Yi, and I. Busch-Vishniac, "Modeling of EAPs as multiple energy domain systems: A bond graph approach." 6168.
[27] T. A. Bowers, [MSc thesis title: Modeling, Simulation, and Control of a Polypyrrole-Based Conducting Polymer Actuator] Massachusetts Institute of Technology, (2004).
[28] A. Maziz, C. Plesse, C. Soyer *et al.*, “Top-down Approach for the Direct Synthesis, Patterning, and Operation of Artificial Micromuscles on Flexible Substrates,” ACS Applied Materials & Interfaces, 8(3), 1559-1564 (2016).
[29] D. Teyssié, C. Chevrot, P.-H. Aubert *et al.*, [Conducting IPNs and Ionic Liquids: Applications to Electroactive Polymer Devices] Springer Berlin Heidelberg, Berlin, Heidelberg %@ 978-3-662-44903-5(2015).
[30] A. Khaldi, A. Maziz, C. Plesse *et al.*, "Patterning innovative conducting interpenetrating polymer network by dry etching." 1424-1429.
[31] F. Meisam, S. Farrokh, N. Naser *et al.*, “Characterization and dynamic charge dependent modeling of conducting polymer trilayer bending,” Smart Materials and Structures, 25(11), 115044 (2016).
[32] H. Jack, [Engineer On A Disk], (2010).
[33] J. D. Madden, P. G. Madden, and I. W. Hunter, "Polypyrrole actuators: modeling and performance." 4329, 72-83.
[34] G. Alici, B. Mui, and C. Cook, “Bending modeling and its experimental verification for conducting polymer actuators dedicated to manipulation applications,” Sensors and Actuators A: Physical, 126(2), 396-404 (2006).
[35] J. D. W. Madden, [PhD thesis title: Conducting Polymer Actuators] Massachusetts Institute of Technology, (2000).
[36] T. Shoa, J. D. W. Madden, T. Mirfakhrai *et al.*, “Electromechanical coupling in polypyrrole sensors and actuators,” Sensors and Actuators, A: Physical, 161(1-2), 127-133 (2010).
[37] S. M. Han, H. Benaroya, and T. Wei, “DYNAMICS OF TRANSVERSELY VIBRATING BEAMS USING FOUR ENGINEERING THEORIES,” Journal of Sound and Vibration, 225(5), 935-988 (1999).
[38] D. C. Karnopp, [Chapter 10: Distributed-parameter systems] JOHN WILEY & SONS, (2012).
[39] T. Sugino, K. Kiyohara, I. Takeuchi *et al.*, “Actuator properties of the complexes composed by carbon nanotube and ionic liquid: The effects of additives,” Sensors and Actuators, B: Chemical, 141(1), 179-186 (2009).